INL/JOU-18-44958-Revision-0

Laser weld-induced formation of amorphous Mn-Si precipitate in 304 stainless steel

Cheng Sun, Emmanuel Perez, Janelle Wharry, Keyou Mao, Yaqiao Wu

August 2018

INL/JOU-18-44958-Revision-0

Laser weld-induced formation of amorphous Mn-Si precipitate in 304 stainless steel

Cheng Sun, Emmanuel Perez, Janelle Wharry, Keyou Mao, Yaqiao Wu

August 2018

Idaho National Laboratory
Idaho Falls, Idaho 83415

http://www.inl.gov

Prepared for the
U.S. Department of Energy
Office of Nuclear Energy
Under DOE Idaho Operations Office
Contract DE-AC07-05ID14517

Laser weld-induced formation of amorphous Mn-Si precipitate in 304 stainless steel

Keyou Mao[1, 2*], Yaqiao Wu[3, 4], Cheng Sun[2], Emmanuel Perez[2], Janelle P. Wharry[1]

[1] Purdue University, 701 West Stadium Avenue, West Lafayette, IN 47907, USA

[2] Materials and Fuels Complex, Idaho National Laboratory, Idaho Falls, ID 83415, USA.

[3] Boise State University, 1910 University Drive, Boise, ID 83725, USA

[4] Center for Advanced Energy Studies, 995 University Blvd, Idaho Falls, ID 83401, USA

* Corresponding Author

Name: Keyou Mao

Postal Address: 701 West Stadium Avenue, West Lafayette, IN 47907, USA

Telephone: +1 765 496 2781

E-Mail Address: kmao@purdue.edu

Abstract

We report the formation of partially amorphous Mn-Si precipitates due to laser welding of face centered cubic (fcc) 304 stainless steel. Transmission electron microscopy and precession electron diffraction studies in the heat affected zone (HAZ) of the weldment indicate the formation of these precipitates in grain interiors. Precipitates have MnSi stoichiometry and the partially crystalline regions have a lattice constant of 0.45 nm. It is surmised that the rapid cooling rates during the laser weld melt pool solidification process may be sufficient to inhibit the complete crystallization of these precipitates.

Graphical abstract

Keywords: amorphous precipitation; precipitation; laser welding; interface; transmission electron microscopy; 304 stainless steel.

Multi-pass laser beam welding is offers a highly concentrated heat source, which enables deeper penetration and higher welding rates, as compared to conventional arc welding techniques. Thus, the process can be used to join thick components with a relatively low heat input, making it a popular technique in numerous industries including automotive, aerospace, petrochemical, and energy. Additionally, the reduced heat input generates a narrow heat affected zone (HAZ) with low residual stress and small distortions. However, after welding, the HAZ experiences a rapid cooling rate ($\sim 10^3$ to 10^7 K/s), which directly controls the solidification mode, and thus has considerable implications on the resultant microstructure [1]. Specifically in austenitic steels, a fine-grained dendritic microstructure is likely to form [2,3], and a phase transformation from austenite to martensite is favorable [4]. However, the predominant phase in the HAZ is austenite with a portion of δ ferrite, dependent on the weld material and solidification mode [5]. The solidification mode is also influenced by the chemical composition within the HAZ, particularly the bulk content of Cr and Ni. Most laser welding phase transformation studies in the archival literature focus on the matrix material, with limited investigation of precipitation or other microstructural features. Thus, in this work, we investigate the microstructure of the HAZ of a 304 stainless steel (SS) weldment, and observe the formation of amorphous precipitates.

Laser welding is performed at Electric Power Research Institute (EPRI) on 304 SS using 308L SS as a filler metal (0.02 inch diameter filler wire) [6]. The neodymium-doped yttrium aluminum garnet (Nd: $Y_3Al_5O_{12}$, abbreviated Nd:YAG) laser is operated using 1 kV weld power, 930 W scan power, 250 mm focal lens, 11.5 inch working distance, and 2 mm spot size. Figure 1 shows an optical micrograph of the cross-section of the 304/308L SS laser weldment, with the base metal, HAZ, and filler metal indicated. The fin-shaped arcs in the filler metal are produced by 183 welding passes. Chemical composition of the base and filler metal is listed in Table 1.

Transmission electron microscopy (TEM), specifically the FEI Tecnai TF30-FEG STwin scanning TEM (STEM), is utilized to evaluate the microstructure change during laser welding. TEM lamellae are prepared by focused ion beam (FIB) lift-out on an FEI Quanta 3D FEG FIB/SEM dual beam microscope. The dimensions of the TEM lamellae are approximately 10 µm × 8 µm × 100 nm; further details of TEM lamellae preparation can be found in reference [7]. Bright field TEM methods are used to image grains and precipitates, whereas dislocations are imaged using two-beam conditions. STEM with energy dispersive x-ray spectroscopy (EDS) is used to analyze the chemical composition of the matrix and precipitates. The thickness of the sample is determined using electron energy loss spectroscopy (EELS). NanoMEGAS ASTAR precession electron diffraction (PED) is used to determine grain and phase orientations.

Bright field TEM images are taken of the base metal (Figure 2a), filler metal (Figure 2b), and HAZ (Figures 2c-f). The bend contours, observed in all three regions of the weldments, arise from residual stresses in the lamellae. Second phases (Figures 2c-e) and dislocations (Figures 2a-c) are readily observed in the micrograph. Based on the Schaeffler diagram [8], the predicted microstructures of the base metal, HAZ, and filler metal are austenite + martensite + ferrite, austenite, and austenite + ferrite, respectively. However, Sufizadeh & Mousavi's results [5] pointed out the fully austenitic microstructure in all the three regions due to the high cooling rate, which changes the solidification mode from ferrite-forming to austenite-forming. Our results corroborate no evidence of martensite or ferrite.

Round precipitates are formed in the HAZ (Figures 2c-e) during the laser welding.

Figures 2c, 2d and 2f show precipitate #1, while Figure 2e shows another precipitate #2 from a different location in the same lamella. The inset diffraction patterns of the two precipitates in Figures 2c and 2e reveal their amorphous nature. The average diameter of the precipitates is 325 ± 110 nm, and the precipitate number density is 3.2×10^{17} #/m^{3} (accounting for the average thickness measured by EELS is 156 nm).

Chemical compositions of the matrix and precipitates in the HAZ, measured by EDS, are summarized in Table 1. The precipitation consists of Si and Mn. There are numerous reports in the archival literature observing formation of $M_{23}C_6$ (fcc) [9], Cr-C (orthorhombic) [5], Cr-N (fcc) [10], NbC (fcc) [11], or Ti-C (fcc) [11,12] precipitates during welding. Typically, these second phases have cubic structures. However, Figures 2c and 2e show the convergent beam electron diffraction (CBED) pattern taken on each precipitate has a diffuse appearance, suggesting the precipitates are amorphous. This finding is consistent with the observation of amorphous Mn-Si phases (partially bcc) by Akgun and Inal [13]. They concluded that the amorphous Mn-Si forms due to the rapid cooling rate after laser surface melting, on the order of ~10^{4}-10^{5} K/s [13]. Similarly, the cooling rate of the weldment studied herein is ~10^{5} K/s, so it is reasonable to expect amorphous Mn-Si precipitation due to cooling rates of this order of magnitude. No such Mn-Si precipitates have been found in the base or filler metals.

The high cooling rate is also expected to produce a higher dislocation density in the HAZ [14]. Bright field and dark field images of dislocation lines are collected under a two-beam condition at zone axis [103] with weak beam where (Figure 3). Using the invisibility criteria, the Burgers vector of the dislocations is determined as 1/2[110]. The counted dislocation density is $3.90 \pm 2.05 \times 10^{13}$ #/m^{2}, which falls on the upper end of the range of typical dislocation densities in 304L SS ~10^{12}-10^{14} #/m^2 [15–17]. Notably, the dislocation density does not change in the immediate vicinity around the Mn-Si precipitates. This result suggests that although both the dislocations and precipitates may arise from rapid cooling, their underlying formation mechanisms differ and are unrelated.

TEM-based PED provides an orientation map (Figures 4a-b) of the grains and Mn-Si precipitate #1. The precipitate appears to be located within a grain with the (101) zone axis in the plane of the image (Figure 4a). Portions of the Mn-Si precipitate are crystalline (see Figure 4a), while the majority of the precipitate volume is amorphous. Considering the Mn-Si phase diagram [18] at the atomic % ratio of Mn to Si ~1 (wt% ratio ~2) and the laser welding temperature >1800 K, we surmise the most likely phase composition of the precipitate to be 50 at% Mn + 50 at% Si [19]. During solidification following laser welding, this composition will pass through the eutectic at 1500 K; if the cooling rate is sufficiently low so as to enable crystallization, the resultant crystal structure closely matches MnSi (cP8, $P2_13$) [19]. High resolution TEM (HRTEM) at various locations along the matrix-precipitate interface shows the transition from fcc (101) matrix to crystalline (118) Mn-Si (Figure 4c) and the direct transition from fcc (101) matrix to amorphous Mn-Si (Figure 4d). By measuring the 1/d-spacing in the HRTEM images, the lattice parameters are determined to be 0.45 nm in the crystalline regions of the Mn-Si precipitates and 0.35 nm in the HAZ matrix.

Precipitation of a crystalline phase requires a sustained kinetic driving force [20]. Often, high-angle (i.e. >50˚) grain or interface boundaries act as a heterogeneous nucleation sites for precipitates, so long as the newly formed phase-matrix interfacial energy is lower than of the original interface [21]. However, the observed Mn-Si precipitates do not form on grain boundaries. Instead, the precipitates form within the HAZ matrix, where the precipitate-matrix interface has high misorientation ranging 15°-180° (Figure 4b). During solidification of the weld melt, the formation of a grain boundary would be in competition with the formation of such a precipitate-matrix interface. Since the average grain boundary energy in >15° misoriented (101) 304 SS is 835 mJ/m^2 at 1333 K, and decreases with increasing temperature [22,23], the critical nucleation energy of crystalline Mn-Si must be >835 mJ/m^2 in order for the precipitate to fully crystallize. The rapid cooling of the laser weldment does not likely supply enough energy to exceed this critical nucleation energy, thus the majority of the Mn-Si precipitate is unable to crystallize and maintains an amorphous structure.

In conclusion, mostly amorphous (partially crystalline) round Mn-Si precipitates are observed in the HAZ of laser welded 304 SS. The precipitates are large (average diameter ~325 nm) and occur at a high number density (~10^{17} $\#/m^3$). The crystalline portions match the MnSi composition and cP8, $P2_13$ structure, with a larger lattice constant than the HAZ matrix. These precipitates are not associated with dislocation nucleation during solidification. Crystallization of the Mn-Si precipitates requires nucleation energy greater than the average grain boundary energy in 304 SS. Rapid cooling of the laser weld melt is not likely to supply sufficient energy to support crystallization. Hence, rapid cooling during the laser welding is an effective approach to create amorphous Mn-Si phases.

Acknowledgments

This research was supported by the Department of Energy Office of Nuclear Energy, contract DE-NE0008525 and the Idaho National Laboratory's Laboratory Directed Research &

Development (LDRD) Program under DOE Idaho Operations Office Contract DE-AC07-05ID14517. The authors thank Jonathan Tatman from the Electric Power Research Institute for providing the welded specimen; Kayla Yano from Purdue University for assistance with TEM lamellae preparation; and Yuhao Wang and Kubra Karayagiz from Texas A&M University for providing information on the Mn-Si phase diagram.

References

[1] N. Kumar, M. Mukherjee, A. Bandyopadhyay, Opt. Laser Technol. 88 (2017) 24–39.

[2] K. Mao, Y. Wu, J.P. Wharry, Microsc. Microanal. 23 (2017) 2212–2213.

[3] K. Mao, H. Wang, Y. Wu, V. Tomar, J.P. Wharry, Mater. Sci. Eng. A (2018).

[4] J.R. Berretta, W. de Rossi, M. David Martins das Neves, I. Alves de Almeida, N. Dias Vieira Junior, Opt. Lasers Eng. 45 (2007) 960–966.

[5] A.R. Sufizadeh, S.A.A. Akbari Mousavi, Int. J. Miner. Metall. Mater. 24 (2017) 538–549.

[6] J. Tatman, in:, Am. Weld. Soc. Laser Conf., San Francisco, 2016.

[7] M.J. Swenson, J.P. Wharry, J. Nucl. Mater. 467 (2015) 97–112.

[8] M.H. Bina, M. Jamali, M. Shamanian, H. Sabet, Int. J. Adv. Manuf. Technol. 75 (2014) 1371–1379.

[9] A.P. Reynolds, W. Tang, T. Gnaupel-Herold, H. Prask, Scr. Mater. 48 (2003) 1289–1294.

[10] N.A. McPherson, K. Chi, T.N. Baker, J. Mater. Process. Technol. 134 (2003) 174–179.

[11] H. Naffakh, M. Shamanian, F. Ashrafizadeh, J. Mater. Process. Technol. 209 (2009) 3628–3639.

[12] M. Sireesha, V. Shankar, S.K. Albert, S. Sundaresan, Mater. Sci. Eng. A 292 (2000) 74–82.

[13] O. V Akgun, O.T. Inal, J. Mater. Sci. 30 (1995) 6097–6104.

[14] F. MALEKGHAINI, M. HAMEDI, M. TORKAMANY, J. SABBAGHZADEH, Scr.

Mater. 56 (2007) 955–958.

[15] M. Tamura, J. Mater. Sci. Res. 6 (2017) 20.

[16] T. Shintani, Y. Murata, Acta Mater. 59 (2011) 4314–4322.

[17] T.S. Sudarshan, T.S. Srivatsan, Rapid Solidification Technology: An Engineering Guide - Google Scholar, CRC Press, 1993.

[18] Gokhale A.B., Abbaschian G.J, Mn-Si (Manganese-Silicon), Second Edi, ASM International, Materials Park, 1990.

[19] J.-E. Jørgensen, S.E. Rasmussen, Powder Diffr. 6 (1991) 194–195.

[20] A. Sutton, R. Balluffi, Interfaces in Crystalline Materials Clarendon, 1995.

[21] L. Priester, in:, Grain Boundaries From Theory to Eng., Springer, Dordrecht, 2013, pp. 217–240.

[22] L.. Murr, G.. Wong, R.. Horylev, Acta Metall. 21 (1973) 595–604.

[23] E.A. TRILLO, E.A. TRILLO, J. Mater. Sci. 33 (1998) 1263–1271.

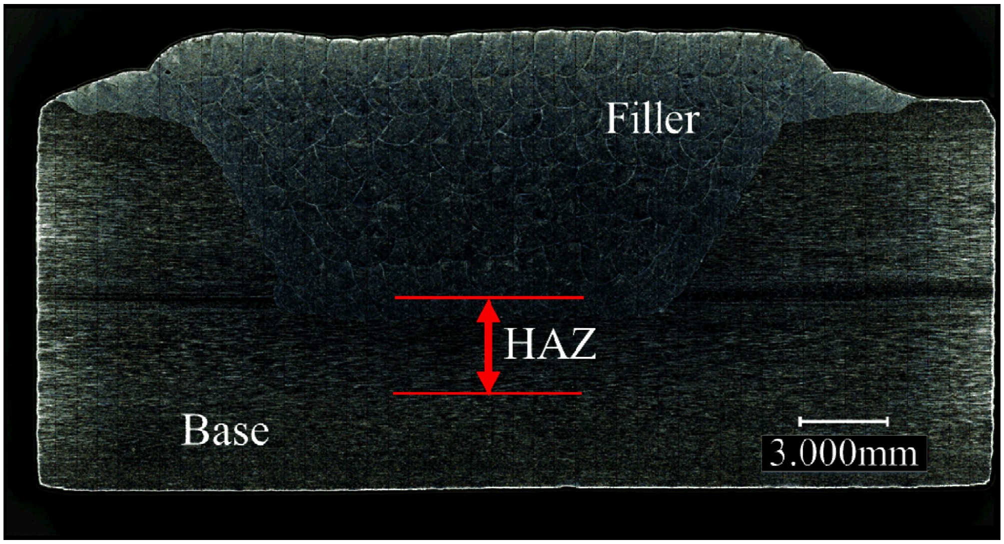

Figure 1 Optical micrograph of the weld.

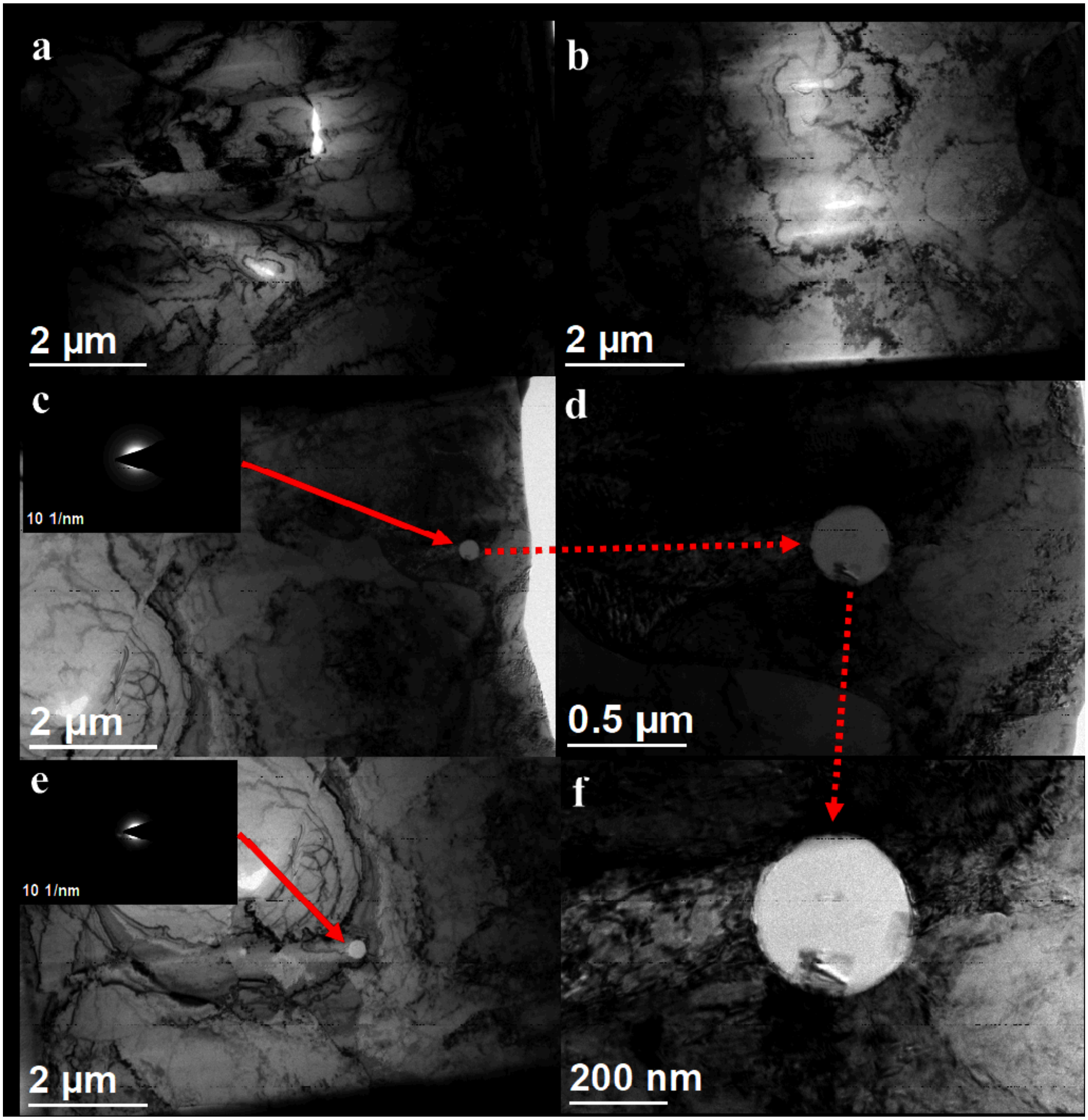

Figure 2 Microstructure of the (a) base metal, (b) filler metal, (c) HAZ with inset CBED pattern of amorphous Si-Mn precipitate 1, (d) detailed image of precipitate 1 (e) HAZ with inset CBED of amorphous Si-Mn precipitate 2 and (f) higher magnification image of precipitate 1.

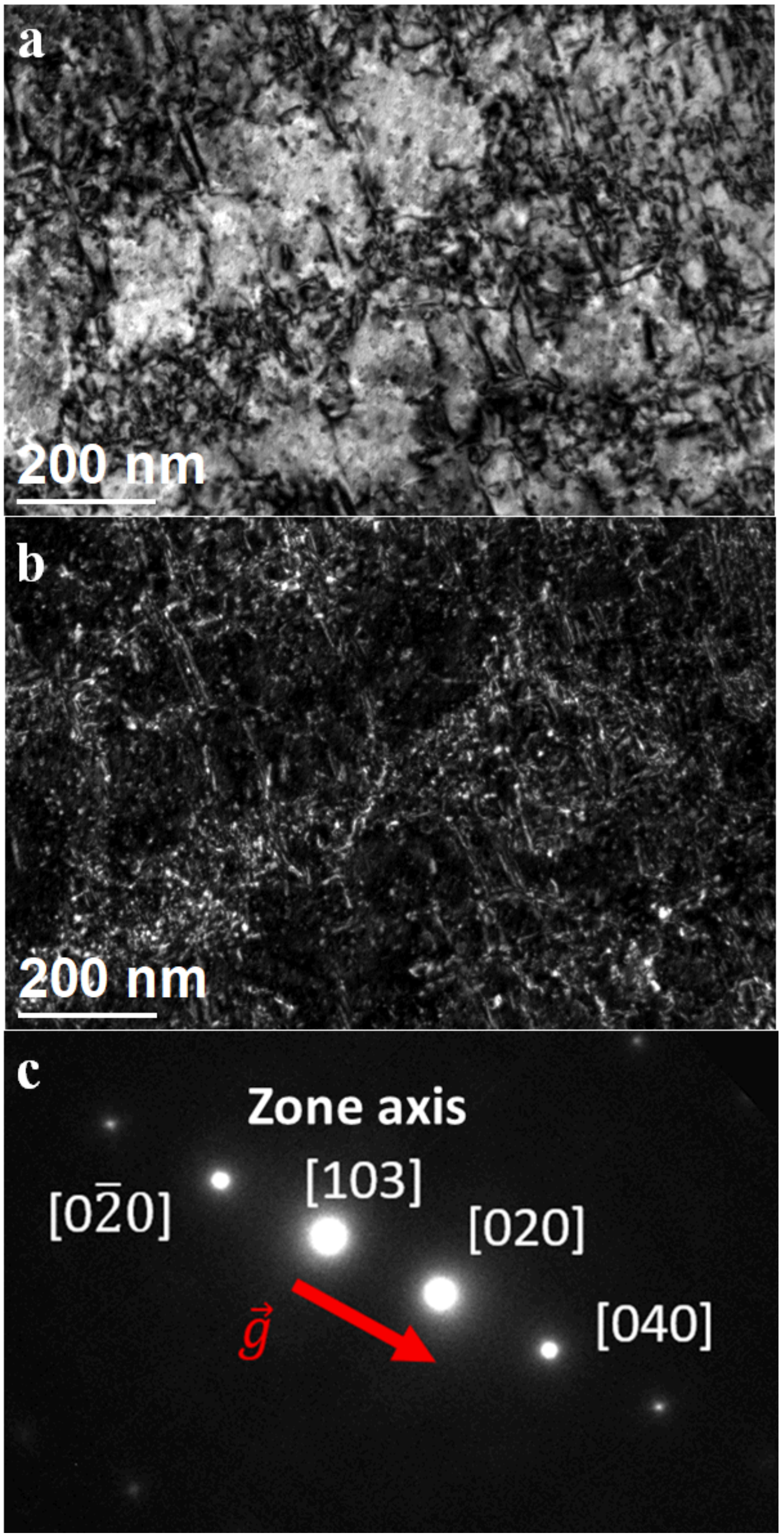

Figure 3 (a) Bright field and (b) dark field images of dislocations in HAZ, taken at (c) zone axis

[103] under two-beam condition with weak beam.

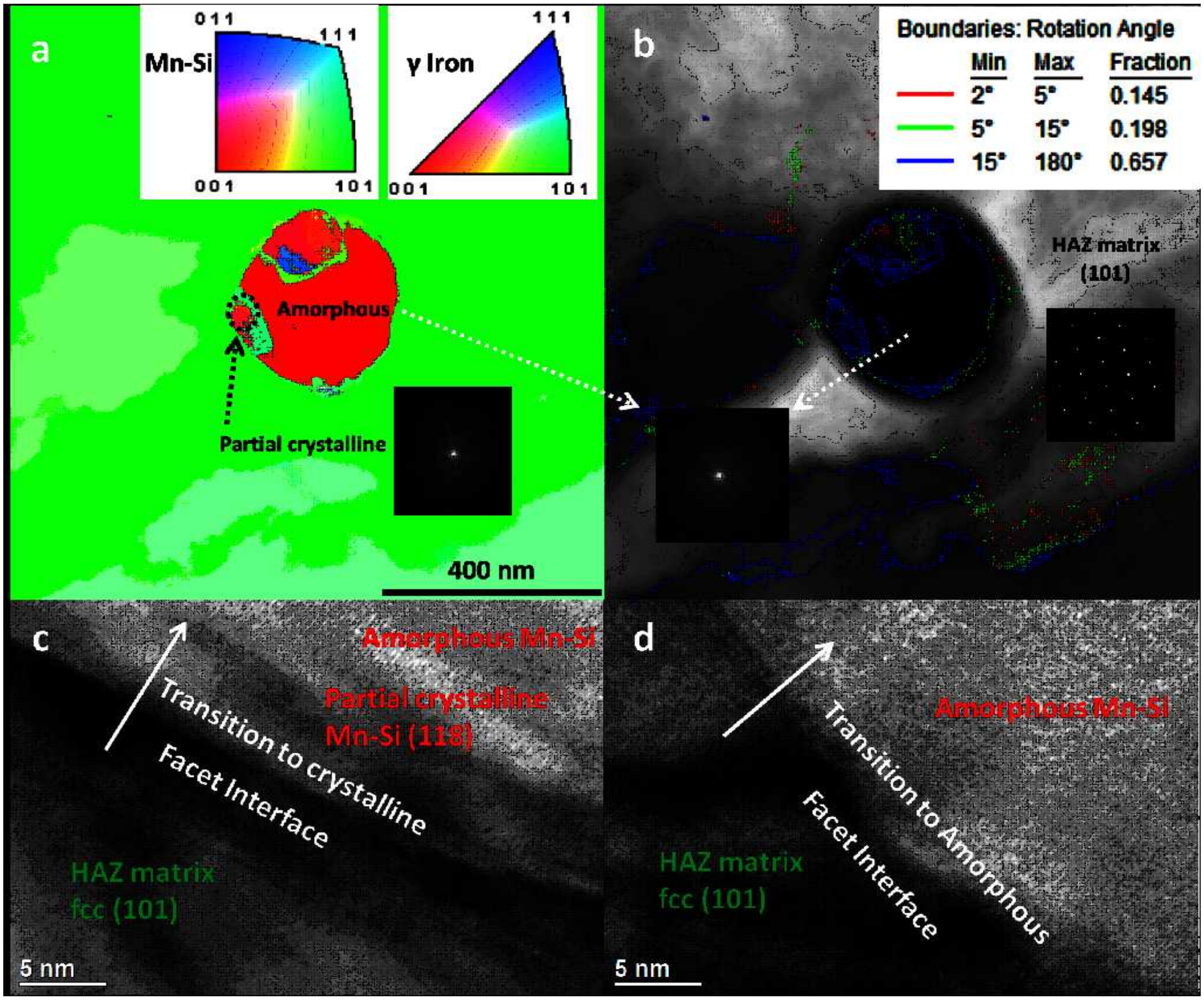

Figure 4 (a) PED grain orientation map and (b) grain orientation angle of Mn-Si precipitate; and HRTEM images of the interface (c) from HAZ matrix fcc (101) to cubic primitive (118) and (d) from fcc (101) to amorphous structure.

Table 1 Chemical composition of the weld material.

Element Wt [%]	C	N	Al	Si	P	S	Ti	Cr	Mn	Fe	Co	Ni	Cu	Nb	Mo	Sn
304L SS	0.018	0.07	0.003	0.34	0.028	0.001	0.003	18.24	1.6	70.63	0.2	8.1	0.37	0.006	0.38	0.008
308L SS	0.021	-	-	0.52	0.023	0.007	-	19.88	2.13	67.53	-	9.79	0.08	-	0.02	-
HAZ (matrix)	0.85	-	0.01	0.14	-	-	-	18.60	1.14	67.97	-	8.04	-	-	-	-
HAZ (precipitate)	4.78	-	2.09	24.54	-	-	-	5.98	53.08	4.21	-	0.25	-	-	-	-